OPEN

Mesoporous hexagonal Co_3O_4 for high performance lithium ion batteries

Dawei Su[1,2], Xiuqiang Xie[2], Paul Munroe[3], Shixue Dou[1] & Guoxiu Wang[2]

[1]Institute for Superconducting and Electronic Materials, University of Wollongong, Wollongong, NSW 2522, Australia, [2]Centre for Clean Energy Technology, School of Chemistry and Forensic Science, University of Technology Sydney, Broadway, Sydney, NSW 2007, Australia, [3]Electron Microscope Unit, University of New South Wales, Sydney, NSW 2052, Australia.

Mesoporous Co_3O_4 nanoplates were successfully prepared by the conversion of hexagonal β-$Co(OH)_2$ nanoplates. TEM, HRTEM and N_2 sorption analysis confirmed the facet crystal structure and inner mesoporous architecture. When applied as anode materials for lithium storage in lithium ion batteries, mesoporous Co_3O_4 nanocrystals delivered a high specific capacity. At 10 C current rate, as-prepared mesoporous Co_3O_4 nanoplates delivered a specific capacity of 1203 mAh/g at first cycle and after 200 cycles it can still maintain a satisfied value (330 mAh/g). From *ex-situ* TEM, SAED and FESEM observation, it was found that mesoporous Co_3O_4 nanoplates were reduced to Li_2O and Co during the discharge process and re-oxidised without losing the mesoporous structure during charge process. Even after 100 cycles, mesoporous Co_3O_4 crystals still preserved their pristine hexagonal shape and mesoporous nanostructure.

Lithium ion batteries are regarded as the most promising power sources for hybrid electric vehicles (HEVs), plug-in hybrid electric vehicles (PHEVs), and energy storage system (ESS) in solar and wind electricity generation[1,2]. However, energy and power densities of current generation lithium ion batteries are limited by cathode materials ($LiCoO_2$) and anode materials (graphite). Transition metal oxides were proposed as high capacity anode materials based on a "conversion" reaction, in which cobalt oxide had demonstrated an excellent electrochemical performance for reversible lithium storage[3]. Since then, various nanostructured transition metal oxides have been investigated as anode materials for lithium ion batteries. Obviously, the performance of lithium storage not only depends on their composition but also on their structure, phase, shape, crystallinity, size, and size distribution[4]. Therefore, control of size and morphology is currently a key issue and numerous studies have been developed to prepare various morphologies Co_3O_4. However, metal oxide anodes usually deliver a low rate capacity due to the slow kinetics of the conversion reaction[5,6]. Recently lots of investigation has been done on the porous or channel structures of the advanced materials with controlled nano/microstructures due to their outstanding properties that are superior to their bulk counterparts[7,8], not except for the mesoporous structure Co_3O_4[9,10]. The Co_3O_4 have been obtained under the help of hard (preformed mesoporous structures) template[11,12], soft (surfactants, hydrogel matrices, block copolymers) template[13] and even the biological ((bacterium, DNA, virus particles, etc.) templates[14]. However, the template-directed synthesis suffers from the disadvantages of low yield and high cost. As an alternative, template-free solution-based synthetic methods have been used to prepared porous nanostructures[15], in which the presence of some inorganic salts ($NH_4H_2PO_4$, Na_2SO_4, Na_2SO_3, NH_4Cl, KCl) are a prerequisite. In addition, the additives and experimental parameters must be carefully selected and controlled.

In this paper, we have employed a solid-state crystal re-construction route to control synthesis of mesoporous Co_3O_4 nanoplates from the β-$Co(OH)_2$ single crystal precursor. In the present strategy the mesoporous structure is generated due to intrinsic crystal contraction, and manifests a well-controlled determinate morphology. When applied as electrode materials, mesoporous facet Co_3O_4 nanocrystals showed an outstanding electrochemical performance as electrode materials in lithium ion batteries with high energy density and power density.

Results and Discussion

Structure and morphological analysis. In the first step of the synthesis, β-$Co(OH)_2$ single crystal nanoplates were prepared by a hydrothermal method using SO_4^{2-} ions as the morphology directing agent. As identified by field emission scanning electron microscopy (FESEM, Fig. 1), the hydrothermal reaction products consist of well-defined nanoplates with a truncated symmetric hexagon pyramid shape. Fig. 2(a) shows the powder X-ray diffraction pattern (XRD) of the β-$Co(OH)_2$ precursor and final Co_3O_4 product. For the precursor
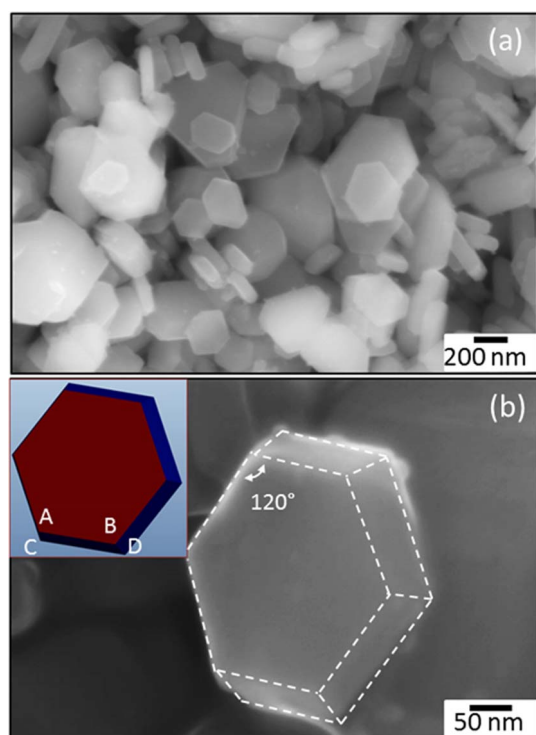
Figure 1 | FESEM images of the as-prepared β-Co(OH)₂ nanoplates, (a) low magnification, and (b) high magnification. The inset of (b) is the corresponding simulated model of β-Co(OH)₂ nanoplates.

β-Co(OH)₂, all diffraction peaks can be fully indexed to the hexagonal symmetry with the space group of PM1 (JCPDS: 30-0443). The XRD pattern of the final Co_3O_4 product exhibits a well-crystalline phase (JCPDS: 65-3103) without any impurity phase, indicating the complete conversion of the precursor. The N_2 sorption isotherm of Co_3O_4 is shown in Fig. 2(b). The hysteresis feature of Co_3O_4 sample can be classified as typical-IV isotherm with an H1-type loop, revealing the mesoporous property of Co_3O_4 product[15]. The pore size distribution curve with only one sharp peak is shown as inset in Fig. 2(b), indicating as-prepared Co_3O_4 has a monomodal pore size distribution with a mean size of 10.89 nm (calculated by the Barrett-Joyner-Halenda (BJH) method). The specific area and total pore volume were determined to be 189.9 m²/g and 1.22 cm³/g, respectively.

The β-Co(OH)₂ nanoplates were further characterised by transmission electron microscopy (TEM) and selected area electron diffraction (SAED) as shown in Fig. 3. It can be seen that they are thin enough to be transparent under the electron beam and display a regular hexagonal shape (Fig. 3 (a)). The lattice resolved HRTEM image presented in Fig. 3(b) illustrates the interplanar distances of the (010) and ($\bar{1}$20) crystal planes (2.75 Å and 1.32 Å, respectively) and an interfacial angle of 150°. The ($\bar{1}$10) and (110) crystal planes with lattice spacing of 2.75 Å and 1.6 Å, respectively, which are perpendicular each other, also can be seen in Fig. 3(b). The SAED pattern taken from this crystal (inset in Fig. 3(b)) can be well indexed along [001] zone axis of hexagonal β-Co(OH)₂, indicating the single crystal feature of as-prepared β-Co(OH)₂ nanocrystals. The clear lattice fringes of (010) and ($\bar{1}$10) crystal planes with a 120° interfacial angle taken from another particle can be observed in Fig. 3(c). Its corresponding SAED pattern also can be indexed along [001] zone axis, confirming as-prepared β-Co(OH)₂ nanocrystals are mainly exposed with {001} crystal planes. According to the symmetries of β-Co(OH)₂, the two hexagon surfaces are the {001} facets and the twelve isosceles trapezoidal surfaces are the {200} and {220} facets. The percentage of the dominant exposed {001} facets to the total
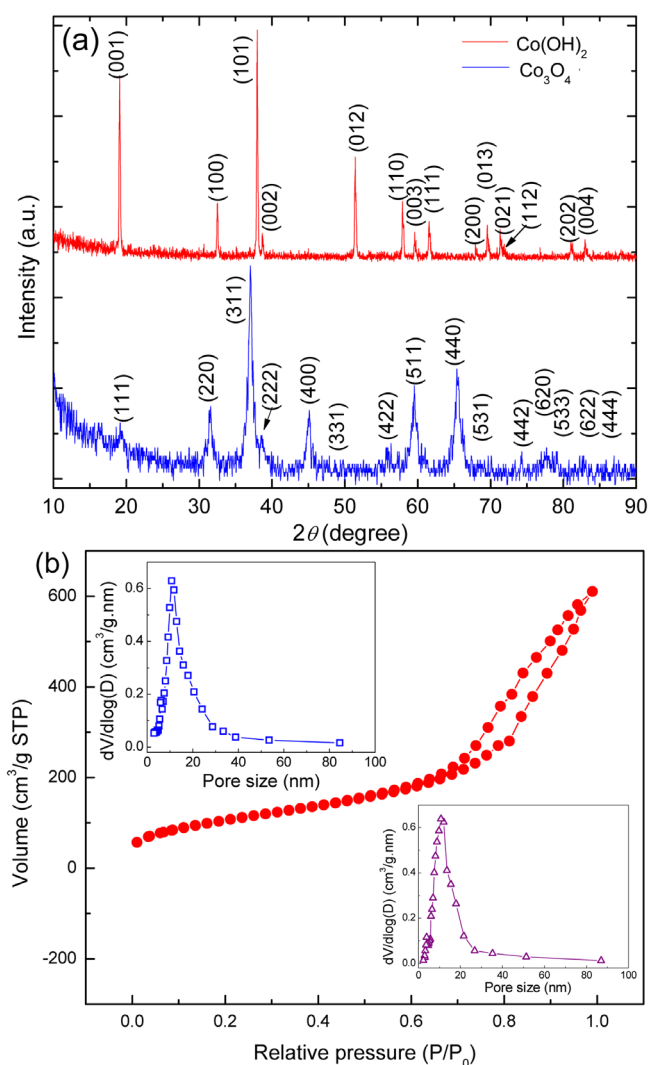
Figure 2 | (a) XRD patterns of the precursor β-Co(OH)₂ and final product Co_3O_4. (b) N_2 isotherms of mesoporous Co_3O_4 nanoplates. The insets show the BJH adsorption pore size distribution plot (top left) and BJH desorption pore size distribution plot (bottom right).

surface area has been calculated to be 78% (see the calculation in Support Information).
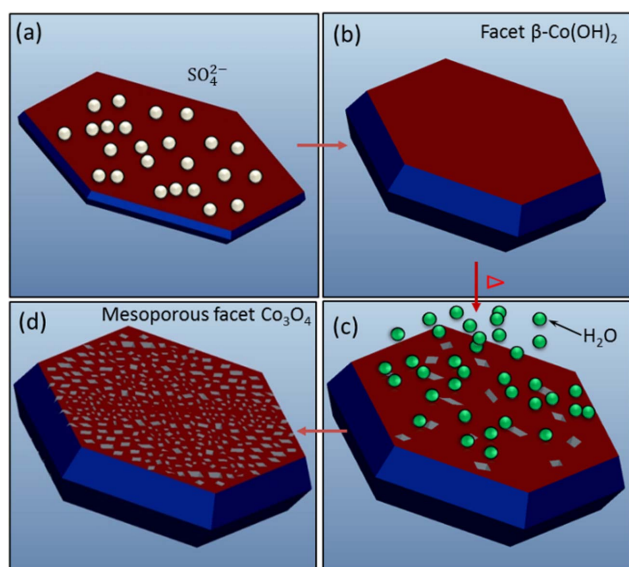
The β-Co(OH)₂ precursor nanoplates were completely converted to Co_3O_4 crystals after annealed at 400°C for 4 h. FESEM observations show that the hexagonal plate shape of β-Co(OH)₂ has been preserved after sintering (Fig. S1, SI). However, the surfaces of Co_3O_4 crystals become much rougher, suggesting the generation of porous structure. The formation process of facet β-Co(OH)₂ nanocrystals and porous facet Co_3O_4 nanocrystals is illustrated in Fig. 4. The first growth step is a nucleation-dissolution and recrystallization process[16]. With the increase of reaction temperature, Co^{2+} ions begin to react with OH^- and form Co(OH)₂ nanocrystals, during which some small metastable block-like precursor crystals were formed immediately due to their intrinsic lamellar structure[17]. The previous study has shown that sulphate ions are most strongly adsorbed to faces perpendicular to the c-axis of the hexagonal crystal system through bridging-bidentate adsorption, leading to the retarded growth along the c-axis and the formation of the facet crystals[18]. Therefore, sulphate ions have a morphology-directing effect in the growth of β-Co(OH)₂ nanoplates. In the second step, β-Co(OH)₂ nanoplates decomposed to water and Co_3O_4 nanocrystals during the sintering treatment. As a result, pores were generated inside and mesoporous structure was formed.
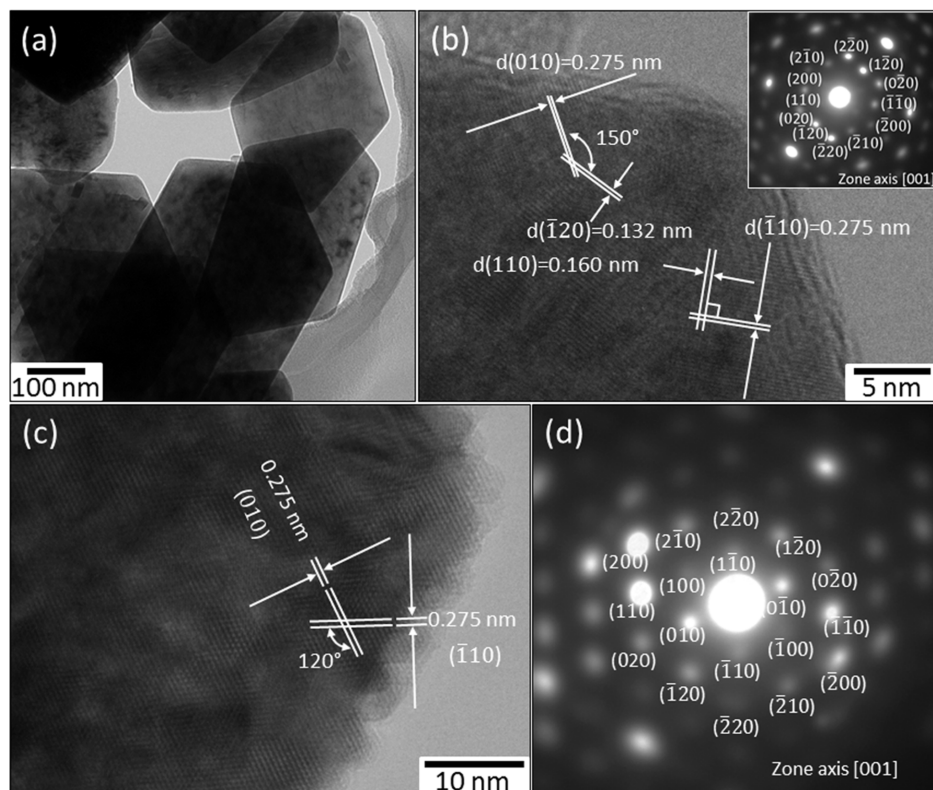
Figure 3 | (a) Low magnification TEM image of β-Co(OH)$_2$ nanoplates. (b) HRTEM image of a β-Co(OH)$_2$ single crystal. The inset is the corresponding SAED. (c) Lattice resolved HRTEM image of β-Co(OH)$_2$ crystal. (d) SAED of the crystal shown in (c).

The morphology and crystal structure of the mesoporous facet Co$_3$O$_4$ nanocrystals were characterised by TEM and HRTEM (Fig. 5). Fig. 5(a) shows a low magnification TEM image, from which we can see that Co$_3$O$_4$ nanoplates have porous architecture with a size of approximately 200 nm. The inset in Fig. 5(a) shows the side view of Co$_3$O$_4$ nanocrystals, indicating the thickness of Co$_3$O$_4$ nanoplates of about 40–50 nm. Fig. 5(b) shows a typical free-standing Co$_3$O$_4$ nanoplate TEM image. The SAED spot patterns (inset of Fig. 5 (b)) taken from this nanocrystal can be indexed along [$\bar{1}$12] zone axis of spinel Co$_3$O$_4$, implying the single crystalline feature of

as-prepared Co$_3$O$_4$ crystals. Fig. 5(c) shows a high magnification TEM image of mesoporous Co$_3$O$_4$ facet crystal, in which the nanoporous nature was illustrated. The Co$_3$O$_4$ single crystals contain inner nanosize pores, which form an integrated porous nano-architecture. The average pore size was determined to be about 10 nm. Fig. 5(d) shows the basal plane of another mesoporous Co$_3$O$_4$ single crystal which was rotated flatly, vertical to the electron beam. The SAED patterns (Fig. 5 (e)) were performed on this nanoplate along [111] zone axis, indicating the major exposed crystal plane of obtained Co$_3$O$_4$ nanoplates is {111}. A lattice resolved HRTEM image showing different crystal planes was recorded by Fig. 5(f), in which we can observe the (111) crystal plane with 4.66 Å d-spacing, (220) crystal plane with 2.85 Å d-spacing (perpendicular to (111)), as well as (311) crystal plane with the smallest d-spacing of 2.43 Å, which is at an angle of 31.5° and 58.5° to the (220) and (111) crystal planes, respectively.

Formation mechanism. The single crystalline of mesoporous Co$_3$O$_4$ nanoplates preserved from precursor β-Co(OH)$_2$ could be resulted from the low mismatch between β-Co(OH)$_2$ (001) crystal plane and Co$_3$O$_4$ (112) crystal plane. When the β-Co(OH)$_2$ nanoplates were re-crystallised and oxidised to Co$_3$O$_4$, the crystal mismatch was strictly controlled within a small range, which is highly favourable for the monocrystallisation process[19]. As shown in Fig. 3, the β-Co(OH)$_2$ nanoplates with the dominant {001} exposed crystal planes have crystal planes of (100), (1$\bar{1}$0), and (0$\bar{1}$0) crystal planes, with the lattice spacings of 2.75 Å, which are very close to the (0$\bar{2}$2), (20$\bar{2}$), and (2$\bar{2}$0) crystal planes (d-spacings are all 2.8 Å) in Co$_3$O$_4$. The crystal mismatch has been calculated to be less than 2% between {001} of β-Co(OH)$_2$ and {111} of Co$_3$O$_4$. Therefore, the single crystalline and facet features were maintained after the conversion from β-Co(OH)$_2$ to Co$_3$O$_4$. The formation of pores in Co$_3$O$_4$ nanoplates originated from matter loss due to thermal decomposition. Compared to the conventional template route[20], the solid-

**Figure 4** | Schematic illustration for the formation of β-Co(OH)$_2$ nanoplates and mesoporous Co$_3$O$_4$ nanoplates.
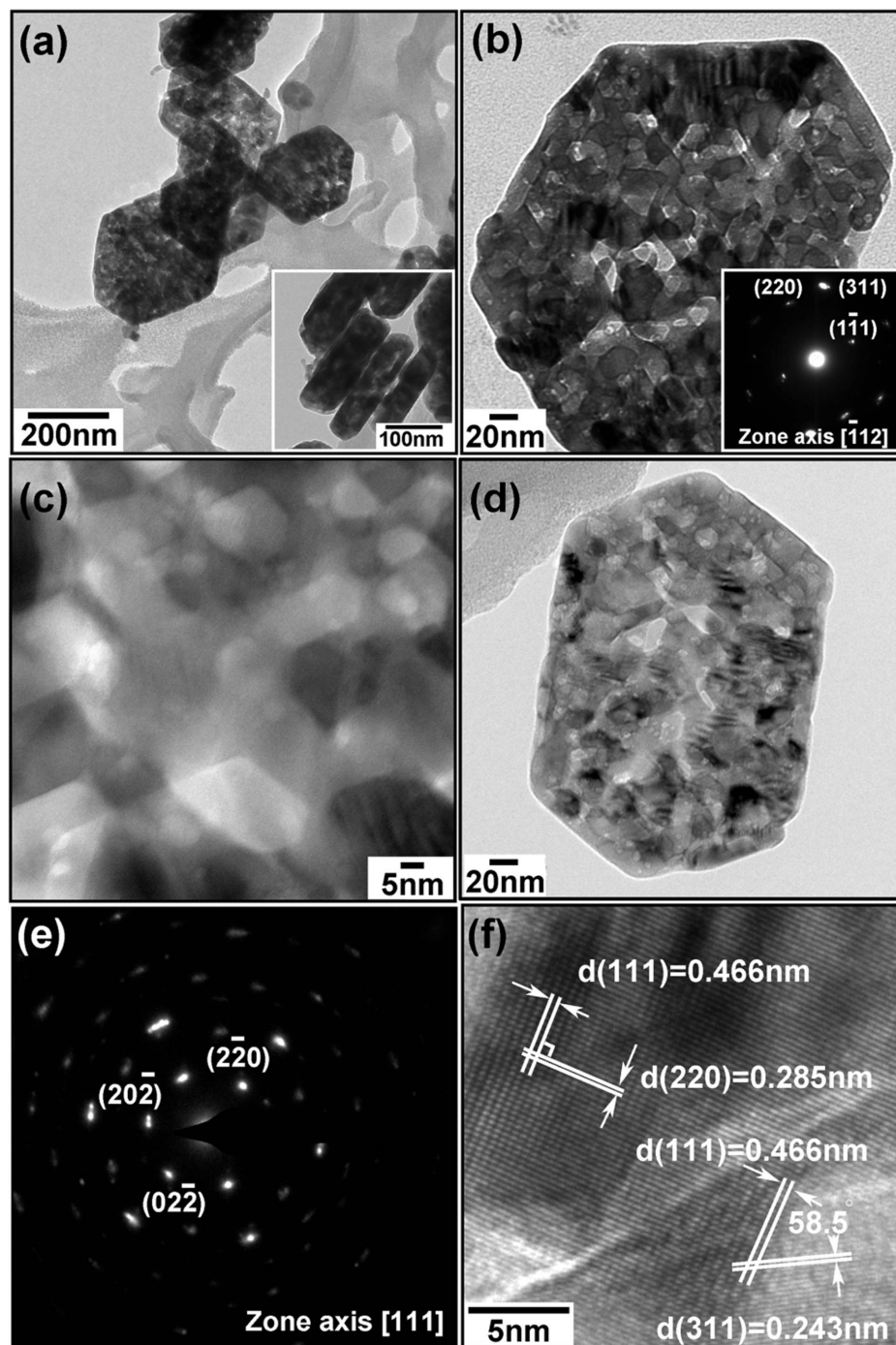
Figure 5 | (a) Low magnification TEM image of mesoporous Co_3O_4 crystals. The inset shows the side view of the facet crystals. (b) High magnification TEM image of a Co_3O_4 nanoplate. The inset is the SAED pattern along the [112] zone axis. (c) HRTEM image of a Co_3O_4 nanoplate, illustrating the mesoporous architecture. (d) Flatly standing Co_3O_4 nanoplate. (e) The SAED patterns taken from (d). (f) Lattice resolved TEM image of Co_3O_4 crystal, from which the lattice spacings of (111), (220) and (311) planes were determined.

state crystal re-construction approach is much more facile and can obtain uniform and robust mesoporous crystals.

Electrochemical performance. The electrochemical properties of mesoporous Co_3O_4 nanoplates for lithium storage were evaluated by cyclic voltammetry (CV) and galvanostatic charge/discharge testing. The CV curves were shown in Fig. S2 (SI), in which the cathodic and anodic peaks are located at 1.1 V and 2.1 V *vs.* Li/Li$^+$, respectively. The CV measurement clearly illustrates the reversible lithium storage in mesoporous Co_3O_4 nanoplates. Fig. 6 shows charge/discharge profiles of mesoporous Co_3O_4 nanoplates at low

current rate (0.05 C). In the first cycle, the electrode delivered a high lithium storage capacity of 2235 mAh/g. It maintained a high reversible capacity from the second cycle and achieved a capacity of 1115 mAh/g in the 100th cycle. It is much higher than the theoretical value (890 mAh/g). The large excess capacity can be ascribed to the decomposition of the electrolyte together with conversion reaction to form an irreversible solid electrolyte inter phase (SEI) layer and further lithium storage via the reversible interfacial charging at metal/Li_2O interface at slope region of lower voltage[11,21,22]. In addition, the high surface area in mesoporous Co_3O_4 nanoplates is favorable to the enhanced efficiency of electrolyte
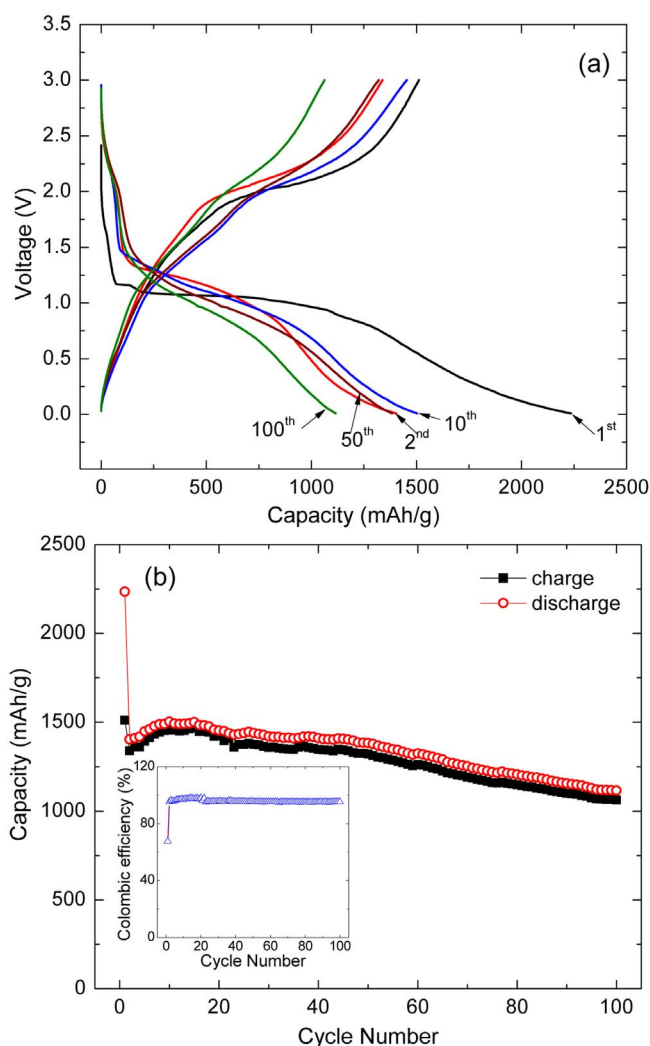
Figure 6 | (a) Charge/discharge profiles of mesoporous Co_3O_4 nanoplates at 0.05 C current rate. (b) Cycling performance of mesoporous Co_3O_4 nanoplates at 0.05 C current rate. The inset of (b) is the corresponding Colombic efficiency.

diffusion and Li ion transport. The uniform pore size distribution at nanoscale and thin Co_3O_4 networks can also contribute to the electrolyte diffusion and serve as the "sponge" to absorb the extra Li ions.

It needs to be noticed that as-prepared mesoporous Co_3O_4 nanoplates demonstrated a good high rate performance. Fig. 7(a) shows the charge and discharge profiles in the 1st, 2nd, 10th, 50th and 100th cycles at 1 C current rate. In the first cycle, the electrode delivered a capacity of 1456 mAh/g. From the second cycle, the electrode maintained high reversibility. The cycling performance of mesoporous Co_3O_4 nanoplates at 1 C is presented in Fig. 7(b). After 100 cycles, the electrode still retained a capacity of 689 mAh/g. The corresponding Coulombic efficiency is shown as the inset in Fig. 7(b). It can be seen that after the initial cycle, the efficiency almost reaches 95%. Even at the 10 C rate, the electrode still delivered a specific capacity of 1203 mAh/g at first cycle as shown in Fig. 7(c). And after 200 cycles, it can still maintain at satisfied value (330 mAh/g). These high rate capacities are higher than the previously reported Co_3O_4 materials with a variety of morphologies[23–25]. Charge/discharge tests were also performed at other current rates. The results are shown in Fig. S3 (SI), which also demonstrates an excellent rate performance. Fig. 7(d) shows the cycling performance of the mesoporous facet Co_3O_4 nanocrystal electrode at varied current rates. It should be

noted that as long as the current rate reverses back low current rate, the cell capacity can almost recover to the original value, indicating the integrity of the electrode has been maintained even after experiencing high rate charge and discharge. This result clearly demonstrates that mesoporous Co_3O_4 nanoplates are tolerant to varied charge and discharge current rates, which is well deserved for high power applications.

Moreover, we compared the electrochemical performance of as-prepared mesoporous hexagonal Co_3O_4 nanoplates with the mesoporous Co_3O_4 syntheized by SBA-15 hard template methode (as shown by Fig. S4, SI). It can be seen that the mesoporous hexagonal Co_3O_4 nanoplates exhibited much better electrochemical performance than the mesoporous Co_3O_4 prepared by the SBA-15 hard template method. Although the SBA-15 mesoporous Co_3O_4 demonstrate the mesoporous structure, it features non-competitive capacity and cyclability under the same testing conditions. Therefore, good electrochemical performance should not only originate from the mesporous architecture, but also should be ascribed to the unique exposed crystal planes. The mesoporous hexagonal Co_3O_4 nanoplates presents a highly active surface due to the predominantly exposed (111) crystal planes[26], which have a large density of low-coordinated atoms situated on steps and kinks, with high reactivity. This favours fast lithium ion transfer between the surface and the interior[27,28].

In order to investigate the lithium-driven structural and morphological changes, we studied as-prepared mesoporous Co_3O_4 nanoplates electrodes at fully discharged (reduced) and charged (oxidized) states after the 1st cycle and 100 cycles at 0.1 C rate (∼89 mA/g current density). We examined the selected-area electron diffraction (SAED) pattern and bright-field images of the samples (as shown in Fig. 8). When Co_3O_4 is fully reduced by lithiation, the bright-field image (Fig. 8 a) shows that the overall shape of the starting particle has been preserved. The Co_3O_4 crystals were reduced by lithium to metallic particles, which are dispersed in a lithia (Li_2O) matrix[3]. The corresponding SAED ring patterns show the presence of Li_2O. The (200), (220) and (311) crystal planes of Li_2O can be well indexed (as shown in Fig. 8 b). The high resolution TEM (HRTEM) image (Fig. 8 c) reveals the formation of the SEI layer on the surface of the particle.

When the electrode is fully charged during the initial cycle, the bright-field image (Fig. 8 d) and the SAED pattern (Fig. 8 e) show different results. The particle has a relatively clear appearance. The mesoporous structure can be readily identified. Taking SAED from the particle, interestingly, we obtained the spot patterns, suggesting the single crystalline feature of the fully charged electrode material. The spot patterns can be well indexed along [111] zone axis of Co_3O_4, which shows the crystalline feature of the Co_3O_4. A lattice resolved HRTEM image (Fig. 8 f) shows the (220) and (022) crystal planes with the lattice spacing of 2.8 Å and 120° angle, which further confirms the well-crystalline of the particle. Mesoporous structure can also be clearly observed. As deduced from the SAED, the first charge process involves in the oxidization of Co to Co_3O_4 and mesoporous facet Co_3O_4 crystals are recovered. This indicates a reversible process during the lithiation and de-lithiation of the Co_3O_4 electrode.

Recently, J.-M tarascon et al. have identified a special mechanism for reversible lithium storage in mesoporous metal oxides (MO), which differs from bulk materials[22]. Mesoporous MO reacts with Li through a conversion reaction, leading to the formation of large metallic M nanoparticles (10 nm) embedded into a Li_2O matrix, together with a copious amount of polymeric materials coming from electrolyte degradation. The polymeric materials surround the particles and fill the pores. Different from bulk MO electrodes, the polymeric layer will be preserved at the end of charge process via capillary effects due to the mesoporosity architecture. As-prepared mesoporous Co_3O_4 crystals match this newly discovered mechanism. And our recently published paper on the mesoporous NiO also showed
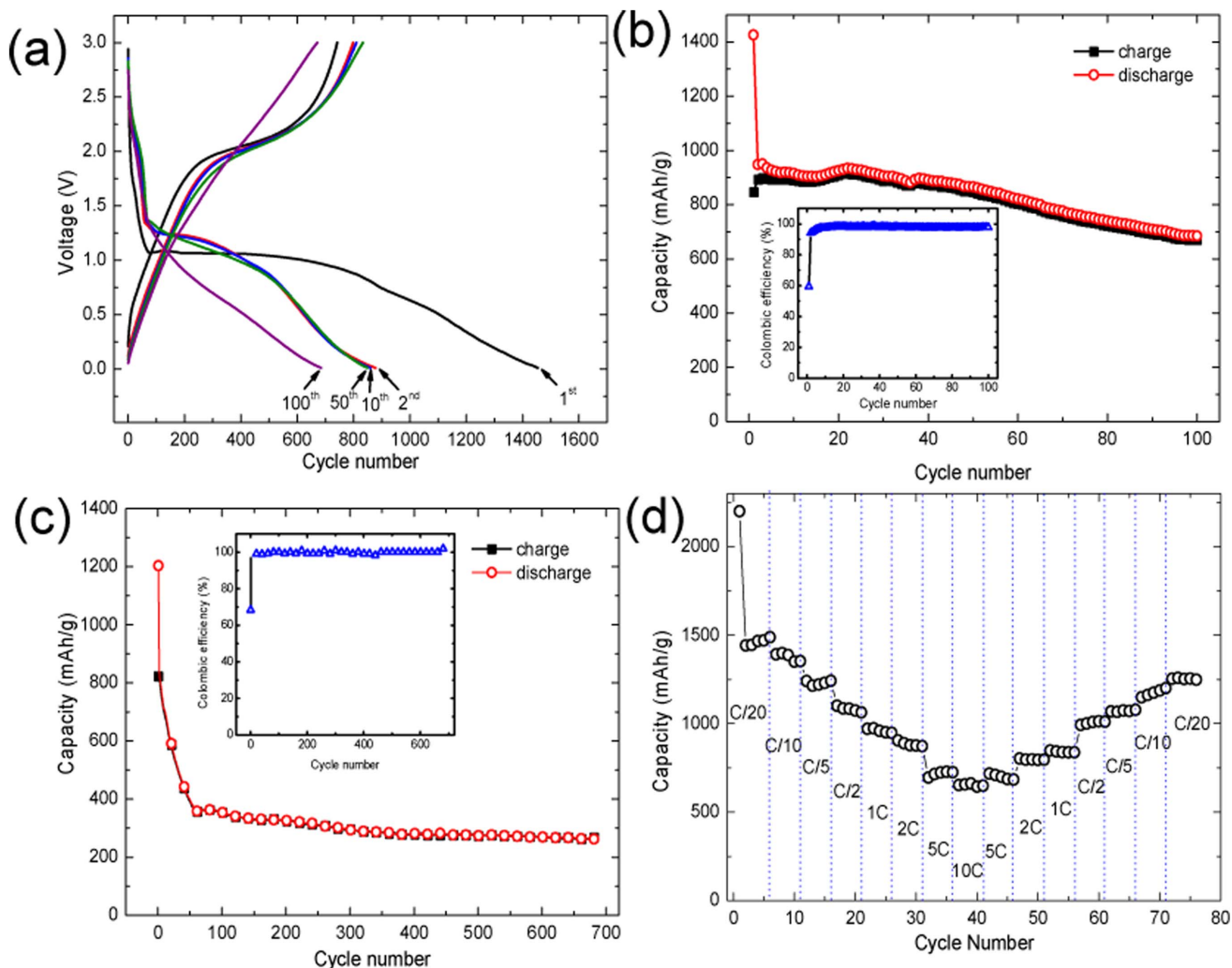
Figure 7 | (a) Discharge and charge profiles of mesoporous Co_3O_4 nanoplates at 1 C current rate. (b) Cycling performance of mesoporous Co_3O_4 nanoplates at 1 C current rate. (c) Discharge capacity vs. cycle number of mesoporous Co_3O_4 nanoplates at 10 C current rate. (d) The rate performance of mesoporous Co_3O_4 crystals at varied current rates. The insets of (b) and (c) show the corresponding Coulombic efficiency.

this phenomenon: the mesoporous structure has been preserved during discharge and charge processes and the exposed {110} facets were restored during charging process[29].

Fig. 8 g, h, and i show TEM images and SAED of the Co_3O_4 crystals at the fully charged state after 100 cycles. It can be seen that the shape of Co_3O_4 nanoplates has been changed. The SAED shows the spot pattern, which can be indexed along [111] zone axis, which illustrates the single crystalline feature of the Co_3O_4 after 100 cycles. From the HRTEM image (Fig. 8 i), we can easily indentify the (220) crystal plane. Fig. S5 (SI) present the FESEM images of the mesoporous Co_3O_4 nanoplates electrode at charged and discharged states, which further identified the SEI layer formed on the fully discharged Co_3O_4 particles in the initial cycle (Fig. S5 (a), SI). When the electrode is fully charged, the Co_3O_4 particles recovered back the original shape and the mesoporous structure is clearly visible (Fig. S5 (b), SI). After 100 cycles, although the Co_3O_4 crystals are covered by the irreversible products, the original hexagonal shape is still maintained (Fig. S5 (c), SI). The *ex-situ* TEM, SAED and FESEM analysis clearly demonstrated that as-prepared mesoporous Co_3O_4 crystals can endure long-time cycling and maintain the mesoporous crystal structure.

Conclusion

Mesoporous Co_3O_4 nanoplates were synthesised by the conversion of hexagonal β-$Co(OH)_2$ nanoplates. TEM, HRTEM and N_2 sorp-

tion analysis confirmed the facet crystal structure and inner mesoporous architecture. When applied as anode materials for lithium storage in lithium ion batteries, mesoporous Co_3O_4 nanoplates delivered a high specific capacity and a good cyclability due to the predominantly exposed {111} reactive facets, uniform pore size distribution at nanoscale and thin nanoplate architecture. The reaction mechanism of facet mesoporous Co_3O_4 crystals was analysed by *ex-situ* TEM, SAED and FESEM observation. It was found that as-prepared mesoporous Co_3O_4 crystals were reduced to Li_2O and Co during the discharge process and re-oxidised to Co_3O_4 crystals without losing the crystallity and mesoporous structure. Even after 100 cycles, mesoporous Co_3O_4 crystals still preserved their pristine hexagonal shape and mesoporous nanostructure.

Experimental Section

Materials preparation. The β-$Co(OH)_2$ single crystal precursors were synthesized by a hydrothermal method. In a typical synthesis process, 2.60 g (0.02 mol) $CoCl_2$ (Sigma-Aldrich, ≥97%) was dissolved in 10 ml distilled water. Then 10 ml 6 M NaOH (Sigma-Aldrich, ≥98%) solution was added under vigorous stirring. After a pink transparent solution was formed, 85.20 mg (0.6 mmol) Na_2SO_4 (Sigma-Aldrich, ≥98%) was added into the solution. The mixture was then transferred into a Teflon-lined autoclave and heated at 120°C for 48 hours in an air-flow electric oven. After cooling to
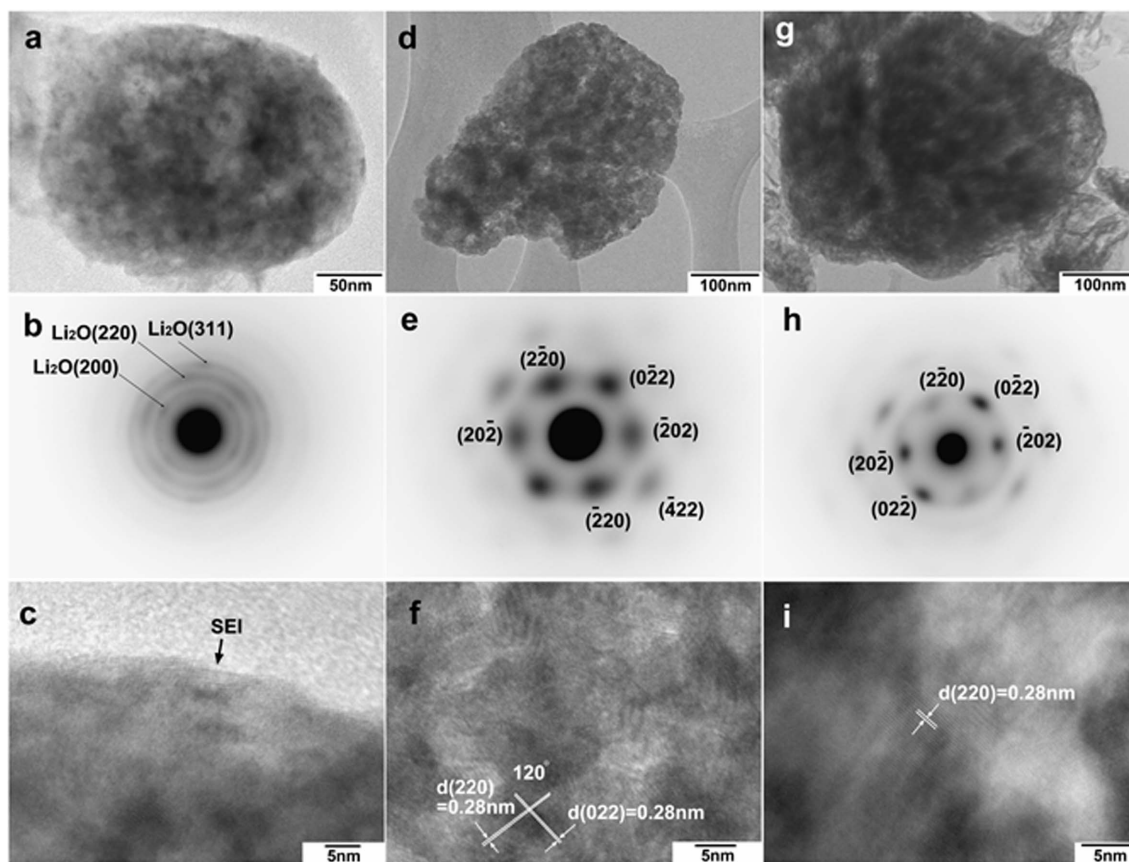
Figure 8 | *Ex-situ* TEM images and SAED patterns of Co₃O₄ electrodes taken from the fully discharged (a–c) and fully charged (d–f) states in the first cycle, and after 100 cycles (g–i). (a), (d), and (g) show individual mesoporous crystals at different states of the reduction and oxidation processes. (b), (e), and (h) are the corresponding SAED patterns. (c), (f), and (i) are the lattice resolved TEM images at various states of the reduction and oxidation processes.

room temperature, the pink product was collected by centrifugation and washed thoroughly with distilled water several times. The β-Co(OH)₂ precursors were obtained after drying for 12 h at 60°C in the vacuum oven. The final mesoporous Co₃O₄ nanocrystals were prepared by annealing β-Co(OH)₂ at 400°C for 4 h in air with a heating rate of 2°C/min. As a comparison, mesoporous Co₃O₄ was synthesized using SBA-15 SiO₂ as hard template.

Materials characterization. The phase of the precursor and final Co₃O₄ nanocrystals were characterised by X-ray diffraction (XRD, Siemens D5000) using a Cu Kα radiation with 2θ ranging from 20° to 90° at a scanning step of 0.02°/sec. The morphologies were analysed by high resolution field emission scanning electron microscopes (FESEM, Zeiss Supra 55VP). The crystal structures were further characterised by transmission electron microscopy (TEM) and high-resolution transmission electron microscopy (HRTEM, JEOL JEM-2011). Selected area electron diffraction (SAED) patterns were recorded by a Gatan CCD camera in a digital format. N₂ adsorption–desorption isotherms were obtained using a Quadrasorb SI analyzer at 77 K. Brunauer–Emmett–Teller (BET) surface area was calculated using experimental points at a relative pressure of $P/P_0 = 0.05–0.25$. The pore size distribution was calculated by the Barret–Joyner–Halenda (BJH) method.

Electrochemical property measurement. The electrodes were prepared by dispersing the as-prepared Co₃O₄ nanocrystals (70 wt%), acetylene carbon black (20 wt%), and poly (vinylidene fluoride) binder (PVDF, 10 wt%) in N-methyl-2-pyrrolidone (NMP) solvent to form a slurry. The resultant slurry was pasted onto copper foil and dried at 100°C for 12 h under vacuum conditions, followed by

pressing at 200 kg/cm². Electrochemical measurements were carried out using two-electrode coin cells with lithium metal as the counter electrode. The lithium metal also works as the reference electrode and the potentials in this work refer to Li/Li⁺. The CR2032-type coin cells were assembled in an argon-filled glove box (UniLab, Mbraun, Germany). The electrolyte solution was 1 M LiPF₆ dissolved in a mixture of ethylene carbonate (EC) and dimethyl carbonate (DMC) with a volume ratio of 1:1. Cyclic voltammetry (CV) was carried out on a CHI 660C electrochemistry workstation with a scan rate of 0.1 mV/s from 0.01 to 3.0 V in a two-electrode system. The charge-discharge measurements were performed at ambient temperature at different current densities in the voltage range from 0.01 to 3.0 V.

To investigate the lithium-driven structural and morphological changes of as-prepared Co₃O₄-based electrodes at various stages of the reduction and oxidation processes, the electrodes were prepared by casting the mixture of as-prepared Co₃O₄ nanocrystals (80 wt.%) and poly (vinylidene fluoride) binder (PVDF, 20 wt.%) in N-methyl-2-pyrrolidone (NMP) solvent only, without acetylene carbon black. A Swagelok type battery was used to test. The cells were charged and discharged to the required voltage and opened in an argon filled glove-box. The electrodes were washed with dimethyl carbonate (DMC) before being placed onto a copper grid mounted on our TEM sample holder.

1. Armand, M. & Tarascon, J.-M. Building better batteries. *Nature* **451**, 652–657 (2008).
2. Bruce, P. G., Scrosati, B. & Tarascon, J. M. Nanomaterials for rechargeable lithium batteries. *Angew. Chem. Int. Ed.* **47**, 2930–2946 (2008).

3. Poizot, P., Laruelle, S., Grugeon, S., Dupont, L. & Tarascon, J. Nano-sized transition-metal oxides as negative-electrode materials for lithium-ion batteries. *Nature* **407**, 496–499 (2000).
4. Sun, Y. & Xia, Y. Shape-controlled synthesis of gold and silver nanoparticles. *Science* **298**, 2176–2179 (2002).
5. Nam, K. T. *et al*. Virus-enabled synthesis and assembly of nanowires for lithium ion battery electrodes. *Science* **312**, 885–888 (2006).
6. Jiao, F. & Bruce, P. G. Mesoporous Crystalline β-MnO$_2$ - a Reversible Positive Electrode for Rechargeable Lithium Batteries. *Adv. Mater.* **19**, 657–660 (2007).
7. Cheng, F., Tao, Z., Liang, J. & Chen, J. Template-directed materials for rechargeable lithium-ion batteries. *Chem. Mater.* **20**, 667–681 (2007).
8. Schüth, F. Endo - and exotemplating to create high-surface-area inorganic materials. *Angew. Chem. Int. Ed.* **42**, 3604–3622 (2003).
9. Lou, X. W. *et al*. Self-Supported Formation of Needlelike Co$_3$O$_4$ Nanotubes and Their Application as Lithium - Ion Battery Electrodes. *Adv. Mater.* **20**, 258–262 (2008).
10. Chen, J. S. *et al*. Shape-controlled synthesis of cobalt-based nanocubes, nanodiscs, and nanoflowers and their comparative lithium-storage properties. *ACS Appl. Mater. Inter.* **2**, 3628–3635 (2010).
11. Wang, Y. *et al*. Weakly Ferromagnetic Ordered Mesoporous Co$_3$O$_4$ Synthesized by Nanocasting from Vinyl-Functionalized Cubic Ia3d Mesoporous Silica. *Adv. Mater.* **17**, 53–56 (2005).
12. Armatas, G. S., Katsoulidis, A. P., Petrakis, D. E., Pomonis, P. J. & Kanatzidis, M. G. Nanocasting of ordered mesoporous Co$_3$O$_4$-based polyoxometalate composite frameworks. *Chem. Mater.* **22**, 5739–5746 (2010).
13. Liu, Y., Zhao, W. & Zhang, X. Soft template synthesis of mesoporous Co$_3$O$_4$/RuO$_2$·H$_2$O composites for electrochemical capacitors. *Electrochim. Acta* **53**, 3296–3304 (2008).
14. Shim, H.-W., Jin, Y.-H., Seo, S.-D., Lee, S.-H. & Kim, D.-W. Highly reversible lithium storage in bacillus subtilis-directed porous Co$_3$O$_4$ nanostructures. *ACS Nano* **5**, 443–449 (2010).
15. Li, Y., Tan, B. & Wu, Y. Freestanding mesoporous quasi-single-crystalline Co$_3$O$_4$ nanowire arrays. *J. Am. Chem. Soc.* **128**, 14258–14259 (2006).
16. Chen, J. S. *et al*. Constructing hierarchical spheres from large ultrathin anatase TiO$_2$ nanosheets with nearly 100% exposed (001) facets for fast reversible lithium storage. *J. Am. Chem. Soc.* **132**, 6124–6130 (2010).
17. Sing, K. *et al*. Physical and biophysical chemistry division commission on colloid and surface chemistry including catalysis. *Pure Appl. Chem.* **57**, 603–619 (1985).
18. Yu, R., Yan, L., Zheng, P., Chen, J. & Xing, X. Controlled synthesis of CeO$_2$ flower-like and well-aligned nanorod hierarchical architectures by a phosphate-assisted hydrothermal route. *J. Phys. Chem. C* **112**, 19896–19900 (2008).
19. Liu, Y. *et al*. Hydrazine route to one-dimensional structural metal selenides crystals. *J. Cryst. Growth* **261**, 508–513 (2004).
20. Zhang, J., Liu, H., Zhan, P., Wang, Z. L. & Ming, N. Controlling the growth and assembly of silver nanoprisms. *Adv. Funct. Mater.* **17**, 1558–1566 (2007).
21. Liang, C., Li, Z. & Dai, S. Mesoporous carbon materials: synthesis and modification. *Angew. Chem. Int. Ed.* **47**, 3696–3717 (2008).
22. Dupont, L. *et al*. Mesoporous Cr$_2$O$_3$ as negative electrode in lithium batteries: TEM study of the texture effect on the polymeric layer formation. *J. Power Sources* **175**, 502–509 (2008).
23. Balaya, P., Li, H., Kienle, L. & Maier, J. Fully reversible homogeneous and heterogeneous Li storage in RuO$_2$ with high capacity. *Adv. Funct. Mater.* **13**, 621–625 (2003).
24. Hu, Y. S., Kienle, L., Guo, Y. G. & Maier, J. High Lithium Electroactivity of Nanometer-Sized Rutile TiO$_2$. *Adv. Mater.* **18**, 1421–1426 (2006).
25. Lou, X. W., Deng, D., Lee, J. Y. & Archer, L. A. Thermal formation of mesoporous single-crystal Co$_3$O$_4$ nano-needles and their lithium storage properties. *J. Mater. Chem.* **18**, 4397–4401 (2008).
26. Zhou, Z.-Y. *et al*. Nanomaterials of high surface energy with exceptional properties in catalysis and energy storage. *Chem. Soc. Rev.* **40**, 4167–4185 (2011).
27. Zhang, D. Q., Wen, M. C., Zhang, P., Zhu, J., Li, G. S. & Li, H. X. Microwave - induced synthesis of porous single - crystal - like TiO$_2$ with excellent lithium storage properties. *Langmuir* **28**, 4543–4547 (2012).
28. Chen, J. S., Liu, H., Qiao, S. Z. & Lou, X. W. Carbon-supported ultra-thin anatase TiO$_2$ nanosheets for fast reversible lithium storage. *J. Mater. Chem.* **21**, 5687–5692 (2011).
29. Su, D., Ford, M. & Wang, G. Mesoporous NiO crystals with dominantly exposed {110} reactive facets for ultrafast lithium storage. *Sci. Rep.* **2**, 924(1)–924(7) (2012).

Acknowledgments

Author contributions

D.-W.S. performed the experiments. X.-Q.X. assisted the experiments. P.M. did the TEM, S.-X.D. and G.-X.W. conceived the study. D.-W.S. wrote the manuscript. All authors discussed the results on the manuscript and reviewed the manuscript.

Additional information